In situ, operando studies on size and structure of supported Pt catalysts under supercritical conditions by simultaneous synchrotron-based x-ray techniques

Journal:	*Physical Chemistry Chemical Physics*
Manuscript ID	CP-ART-01-2019-000347.R2
Article Type:	Paper
Date Submitted by the Author:	01-May-2019
Complete List of Authors:	Lee, Sungwon; Argonne National Laboratory, Materials Science Division Lee, Sungsik; Argonne National Laboratory, Gerceker, Duygu; University of Wisconsin-Madison, Chemical and Biological Engineering Kumbhalkar, Mrunmayi; University of Wisconsin, Chemical and Biological Engineering Wiaderek, Kamila; Argonne National Laboratory, X-ray Science Division Ball, Madelyn; University of Wisconsin, Chemical and Biological Engineering Mavrikakis, Manos ; University fo Wisconsin - Madison, Dumesic, James; University of Wisconsin, Chemical and Biological Engineering Winans, Randall; Argonne National Laboratory, X-ray Science Division; ory

Journal Name

ARTICLE

In situ, operando studies on size and structure of supported Pt catalysts under supercritical conditions by simultaneous synchrotron-based x-ray techniques

Received 00th January 20xx,
Accepted 00th January 20xx

DOI: 10.1039/x0xx00000x

www.rsc.org/

Sungwon Lee,[a] Sungsik Lee,[a] Duygu Gerceker, [b] Mrunmayi D. Kumbhalkar,[b] Kamila M. Wiaderek,[a] Madelyn R. Ball,[b] Manos Mavrikakis,[b] James A. Dumesic,[b] Randall E. Winans*[a]

To control the size and structure of supported Pt catalysts, the influence of additional metal particles and the effect of the support were elucidated during the cracking reaction of n-dodecane under supercritical reaction conditions. The dynamical changes in nanocatalysts and catalytic activity are studied under realistic reaction conditions by using a combination of simultaneous temperature-programmed heating, in-situ Small Angle X-ray Scattering (SAXS) and X-ray Absorption Near Edge Structure (XANES). *In situ* SAXS results indicate that the stability of the catalysts increases with Sn concentration. *In situ* XANES analysis reveals that the degree of oxidation and electronic state of catalysts are dependent on the amount of Sn. Carbonaceous deposits over spent catalysts were characterized by Raman spectroscopy, indicating that the highest Sn loading inhibits the formation of disordered graphitic lattices, which leads to an increased catalytic activity. SiO_2, γ-Al_2O_3 and $Mg(Al)O_x$ were employed as supports to investigate the support effect on the stability of Pt catalysts. *in-situ* SAXS and XANES results clearly show the improved stability of catalysts on γ-Al_2O_3 and $Mg(Al)O_x$ supports compared to Pt catalysts on SiO_2 and electronic state of catalysts are strongly influenced by support materials.

1. Introduction

As an aircraft speed increases to the hypersonic regime, thermal management becomes a key issue in the vehicle and engine development due to the increased aerodynamic heat.[1] For instance, the temperature of external air of supersonic combustion ramjet (scramjet) can reach up to 4950 K at Mach 12, often leading the failure of the metal material of the engines.[2] Cryogenic fuels, such as liquid methane or hydrogen, can provide sufficient cooling; however, they require enormous vehicle capacity as well as additional safety and operational caution. Hydrocarbon fuels have been considered as a coolant, by flowing through cooling channels to cool the engine walls. To overcome the heat load with high flight Mach number, endothermic hydrocarbon fuels have to be used to provide sufficient heat sink for the cooling. From a practical point of view, one drawback is the formation of carbonaceous deposits under supercritical conditions, which clogs the fuel systems and causes engine failures.[3] Much work has been done to overcome this limitation[4-7] and catalytic cracking is receiving significant attention since it can not only lower the reaction temperature, but also change the reaction pathways by reducing pyrolysis.[8]

Pt catalysts[9, 10] are widely used in commercial catalytic processes such as dehydrogenation,[11-13] hydrogenation,[14] and automobile exhaust.[15] The Pt-Sn bimetallic catalytic system has shown synergistic effects due to the unique physicochemical properties of the two metals, leading to improved stability and selectivity.[16-25] Merlen and coworkers reported the physical properties of bimetallic Pt-Sn/Al_2O_3 catalysts by studying the relationship between particle size and structure.[19] Lee and coworkers reported the dehydrogenation of propane by PtSn/θ-Al_2O_3 catalysts with different amounts of Sn.[20] Recently, Pt-Sn/Mg-Al-O catalysts were employed for the dehydrogenation of long chain paraffin (n-dodecane) and investigated the support effect by controlling the amount of Mg.[21] However, to the best of our knowledge, little work has been done on the investigation of the particle size and structure changes for bimetallic catalysts during cracking reaction at realistic supercritical conditions.

Many studies have been focused on the noble metal or alloys to provide superior catalytic activity[14, 15, 21] but there are not extensive studies looking at the support system. It is reported that mixed oxides can provide good mechanical strength and can be tailored to achieve better selectivity.[26] The metal-oxide interaction such as electron or oxygen transfer can improve the performance of supported catalysts.[27, 28] Adding Mg to support leads to many advantages including the weakening the acid sites and increased Pt-support interaction.[14] Belskaya and coworkers reported that 90% of the n-decene

[a] X-ray Science Division, Argonne National Laboratory, 9700 S. Cass Ave., Lemont, IL 60439 United States
[b] Department of Chemistry and Biological Engineering, University of Wisconsin, Madison, WI 53706 United States
E-mail: rewinans@anl.gov
Electronic Supplementary Information (ESI) available: See DOI: 10.1039/x0xx00000x

formation selectivity achieved by tailoring support material without a modifier added.[29] We recently reported the particle size and structural variation of Pt catalysts supported on SiO_2 during the endothermic cracking and dehydrogenation of n-dodecane, suggesting that controlling the size and geometric structure of platinum nanocatalysts could lead to a fundamentally new level of understanding of nanoscale materials in realistic reaction condition.[9]

In the present work, we have focused on elucidation of particle size and structure of supported Pt catalysts with the influence of additional metal particles and the effect of the support nanostructure. Therefore, the objectives of this paper are (1) to study the effect of Sn loading on Pt-Sn/SiO_2 bimetallic catalysts and (2) to elucidate the effect of support materials, γ-Al_2O_3 and Mg(Al)O_x on Pt catalysts for the catalytic cracking and dehydrogenation of endothermic hydrocarbon fuels under supercritical conditions (over T_c=385 °C, P_c=260 psi). The properties of Pt-Sn catalysts and the supported Pt catalysts were characterized by synchrotron-based small angle X-ray scattering (SAXS) and X-ray Absorption Near Edge Structure (XANES). These techniques are some of the most powerful methods for characterizing highly dispersed metal catalysts which are very difficult to study by other techniques.[30] As a model fuel, n-dodecane was chosen since it has been often used to represent one of the major components of petroleum-derived jet fuels.[31] The cracking of n-dodecane as an endothermic hydrocarbon fuel in a flow cell reactor was carried out under supercritical conditions. Raman spectroscopy was employed to analyze the spent catalysts with a focus on coke precursor species. GC/MSD (Gas chromatography–mass spectrometry detector) was employed to analyze the liquid products collected at various stages of the reaction. The reactant conversion and reaction selectivity were determined by analyzing the product distribution quantitatively.

2. Experimental

2.1 Catalysts preparation and characterization

Silica-supported platinum catalysts were prepared by ion exchange using the method of Benesi *et al*[32]. After ion exchange, the resulting Pt/SiO_2 was filtered, washed with deionized water and dried at 110 °C. This synthesis was followed by first calcining the catalyst at 300 °C for 2 h and then reducing it in flowing hydrogen for 2 h at 400 °C. To prepare the Pt/γ-Al_2O_3 catalysts, the incipient wetness impregnation method was used. Tetraammineplatinum (II) nitrate was dissolved in deionized water and added to the γ-Al_2O_3 support dropwise. After drying overnight at 110°C, the catalyst was calcined under flowing air at 450°C for 2 h, and was reduced under flowing hydrogen for 2 h. Subsequently, the catalyst was passivated under flowing 1% O_2 for 1 h. Pt/Mg(Al)O_x catalysts were also prepared by incipient wetness impregnation. Prior to the impregnation step, the Mg:Al = 3:1 hydrotalcite was calcined at 500 °C. Following the Pt impregnation, same pretreatment procedure as with the Pt/γ-Al_2O_3 catalyst was performed. A Perkin-Elmer Plasma 400 ICP Emission Spectrometer was used to determine the Pt metal loading on the support. Sequential impregnation of Sn was carried out by evaporation using tributyltin acetate in pentane solution. The catalyst was then dried, calcined at 300 °C for 2 h, and reduced at 400 °C for 2 h in this sequence. The catalyst composition and CO chemisorption uptakes are shown in Table 1. *Ex situ* catalyst characterization to determine average particle size and distribution was performed using scanning transmission electron microscopy. For imaging, a high-angle annular dark-field (HAADF) Z-contrast STEM (FEI Titan operated at 200 kV) was used. As seen in Figure S1, the majority of particles for fresh Pt/SiO_2 and Pt-Sn/SiO_2 were 1~2 nm in diameter.

Table 1. Elemental composition of the Pt-Sn/SiO_2 catalysts

Sample	Pt (wt%)	Sn (wt%)[a]	CO Uptake (μmole/g)[b]
Pt	1.9	0	100
Pt_3Sn_1	2.4	0.5	70
Pt_1Sn_1	1.9	1.2	37
Pt_1Sn_3	1.9	3.4	25

[a] Theoretical values
[b] Error is ± 0.5 μmole/g

2.2 In situ catalytic cracking experiments

Catalysts (ca. 1.5 mg) were loaded into a sapphire capillary (1.5 OD x 1.0 mm ID, Saint-Gobain Crystals, Hiram, OH) and mounted in a flow reaction cell, equipped with a high pressure syringe pump (Teledyne ISCO, Lincoln, NE). n-Dodecane (> 99%) from Sigma-Aldrich was used as received. The reaction temperature was controlled by a custom made heater[9] and a temperature controller (Eurotherm 2404) in the range of 25 - 600 °C. Stainless steel tubing (60 cm length, 0.05 mm ID x 0.3 mm OD) was used as the back-pressure generator. The initial stage of reaction started with a flow rate of 0.01 mL/min under constant pressure of 750 psi at 25 °C. Then the flow rate gradually decreased and reached 0.005 mL/ml at 600 °C to maintain the constant pressure. *in situ,* operando SAXS and XANES measurements were carried out during the reaction at various pressure and temperature conditions at beamline 12-BM of the Advanced Photon Source (APS) at Argonne National Laboratory. SAXS measurements were made at 11.5 keV by using an area detector (MarCCD 165). Silver behenate was used for calibration. XANES data were collected at the Pt-$L_{2,3}$ edges in fluorescence mode at room temperature using a 13 elements germanium detector. The energy was calibrated using a platinum foil (Pt-L_2 edge = 13,273 eV; Pt-L_3 edge = 11,564 eV). The liquid products were collected at each reaction condition and stored for further characterization.

2.3 Catalytic activity measurements and data analysis

Post-experimental Raman spectroscopy was carried out with a Ranishaw inVia Raman microscope system in the Center for Nanoscale Materials (CNM) at Argonne National Laboratory. The spent catalysts were retrieved after the cracking reaction and analyzed with 514 nm laser at ambient condition. The liquid products were identified using an Agilent 7890A gas chromatograph, which was equipped with an Agilent 5975C MSD. A capillary column coated with (5%-Phenyl)-methyl-polysiloxane was used for all analyses (HP-5MS, 30 m x 0.25

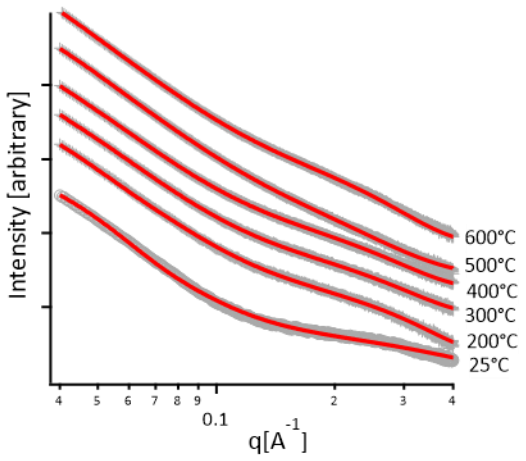

Figure 1. Background corrected *in situ* SAXS scattering profiles of Pt-Sn/SiO_2 catalysts (Pt_3Sn_1) in the temperature range of 25 to 600 °C at 750 psi with n-dodecane. (Gray circles: raw data, red line: model curve fitting)

mm, Agilent technologies). Helium was used as the carrier gas and the injection volume was ca. 0.2 μL with 1/100 split. Naphthalene-*D8* was used as an internal standard for the quantitative analysis by using total ion chromatogram (TIC) area ratio. To determine the percent yield of conversion, a calibration curve (R^2 >0.9) with known solutions of n-dodecane was used. The SAXS scattering profiles were integrated by azimuthal integration and analyzed by using the Irena software package.[33] To determine the size distribution of catalyst particles, a SAXS scattering intensity was fitted by using Modeling II (Irena) under two populations, assumed with the Schultz-Zimm distribution of spherical particles (aspect ratio = 1). Data processing in the XANES region was performed with the Athena software package [34], where the spectra were calibrated, averaged, and normalized. For Raman analysis, linear baseline correction and band fitting was carried out by using PeakFit software. (v4.12, Systat Software Inc.) By using Lorentzian shapes, an optimal fit was obtained with r^2>0.998.

3. Results and discussion

3.1 Effect of tin as a promoter

Figure 1 shows the representative SAXS scattering intensities and the fitting results of the Pt-Sn/SiO_2 bimetallic catalyst (Pt_3Sn_1) in the temperature range of 25 – 600 °C at 750 psi with n-dodecane. (The fitting results for Pt, Pt_1Sn_1, and Pt_1Sn_3 are shown in Figure S2) A broad scattering peak appears in the high q region (0.2<q<0.4, $Å^{-1}$) at ambient temperature, indicating the presence of nanoparticles. This peak started to shift to the low q range as the temperature increases. The shift in scattering peak to the lower q regime was continued on successive measurements, indicating the increase of the particle size as temperature increases. The corresponding particle size (mean diameter, Å) and the size distribution profiles are illustrated in Figure 2. Without Sn (Pt, Figure 2(A)), the particle size was 11.9 ± 0.9 Å at 25 °C but increased up to ca. 23.5 ± 0.7 Å when reaction temperature reached over the critical condition (T_c=385 °C). However, the addition of Sn to Pt/SiO_2 supported catalysts shows a significant effect on their stability against sintering during the cracking process. The initial particle diameters (at 25 °C) of Pt_3Sn_1, Pt_1Sn_1, and Pt_1Sn_3

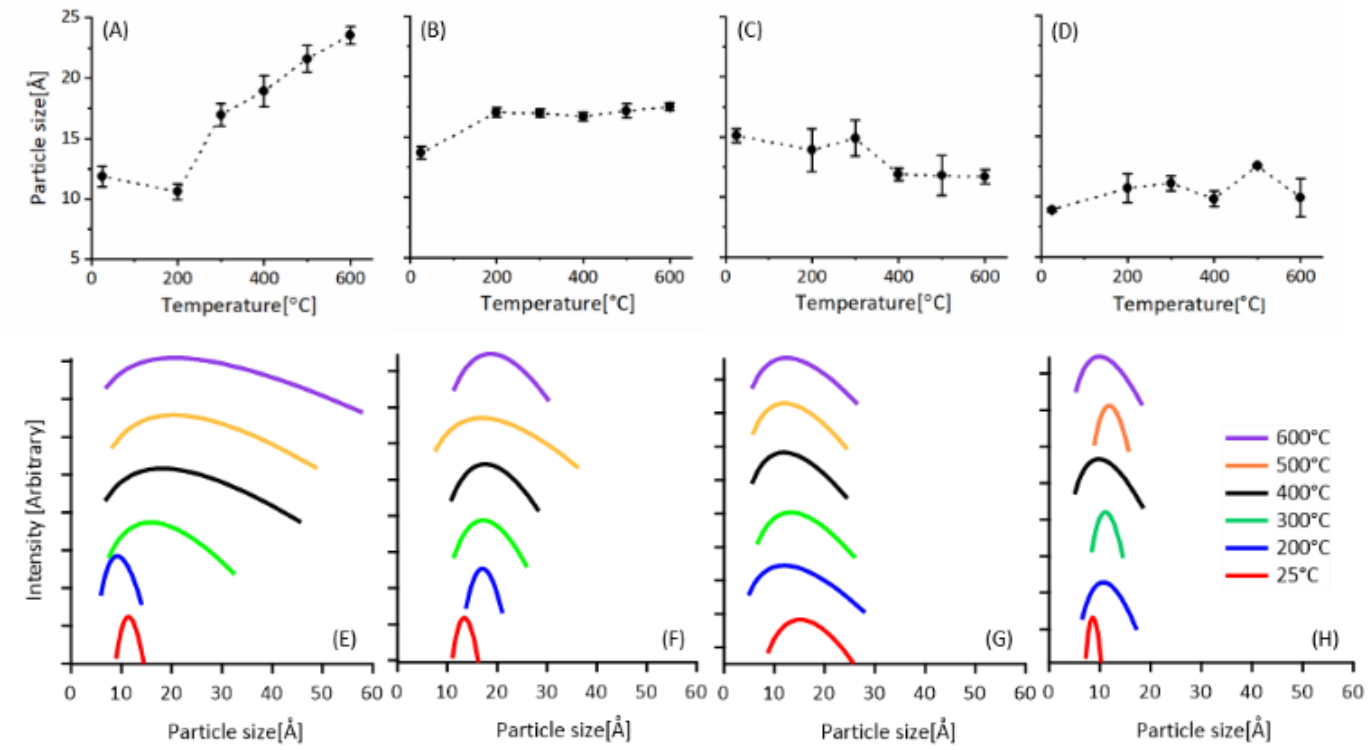

Figure 2. Variation of particle size of Pt-Sn/SiO_2 catalysts (A) Pt (B) Pt_3Sn_1 (C) Pt_1Sn_1 (D) Pt_1Sn_3 with n-dodecane present. The corresponding size distribution profiles of Pt-Sn/SiO_2 catalysts (E) Pt (F) Pt_3Sn_1 (G) Pt_1Sn_1 (H) Pt_1Sn_3

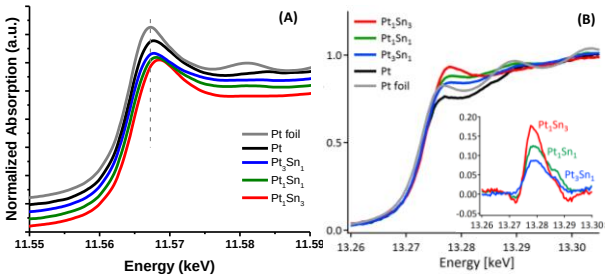

Figure 3. (A) Pt L_3 XANES and (B) Pt L_2 XANES data of Pt-Sn/SiO_2 catalysts Pt, Pt_3Sn_1, Pt_1Sn_1, Pt_1Sn_3 and Pt foil after reduction under H_2. Inset; ΔXANES (catalysts XANES – Pt XANES)

catalysts were 13.7 ± 0.5, 15.1 ± 0.6, and 8.9 ± 0.2 Å, respectively. The particle size of each catalyst, after the temperature reached over the supercritical condition, were merely changed to 17.5 ± 0.3, 11.7 ± 0.6, and 9.9 ± 1.6 Å, respectively. There was a sudden increase in particle size of the Pt_1Sn_3 catalyst when the temperature reached at 500 °C. Overall, the size and the variation upon temperature increase were smaller as the amount of Sn was increased, clearly showing increased stability under supercritical conditions. The size distribution profiles in Figure 2 (E-H) emphasize the effect of Sn on the Pt catalyst. Without Sn addition, the size distribution of monometallic Pt catalyst has dramatically increased as temperature increased, as shown in Figure 2(E). The addition of Sn increases catalyst stability, showing that the variation in size distribution of Pt_1Sn_3, the highest amount of Sn among the prepared catalysts, is clearly reduced as temperature increases, as compared to those of the Pt catalyst.

To better understand the interplay between morphology and catalytic reaction under supercritical environments, XANES characterization was employed to measure the electronic states above the Fermi level localized on Platinum. XANES characterization was also performed in ambient conditions with samples as received. Figure 3 shows the Pt L_3 and L_2 edge XANES spectra of Pt-Sn/SiO_2 bimetallic catalysts after being reduced with hydrogen gas (4% H_2 in He) at 250 °C. All measurements were performed at room temperature with inert gas environment (UHP helium). The white line of the $L_{2,3}$-edge of the Pt metal is used as an important parameter, since it is mainly associated with density of unoccupied 5d electronic states of Pt. Figure 3 (A). It shows the systematic edge change of Pt L_3 edge toward higher energy as Sn content is increased (Pt < Pt_3Sn_1 < Pt_1Sn_1 < Pt_1Sn_3), which indicates a higher final state of unoccupied Pt 5d electron induced by partial filling of the unoccupied Pt 5d orbitals from Sn. High degree of edge shift toward higher energy in Sn XANES spectra shown in Figure S4 also support this. The white line intensity of L_3 edge shows no significant change as Sn content changes. Fourier transform magnitudes of Pt L3 edge EXAFS spectra and fit results are shown in Figure S3, which indicates low coordination number and broadening of feature attributed from Pt-Sn bond formation. A full list of coordination conditions obtained by fitting the EXAFS data can be found in Table S1. Figure 3 (B) shows the Pt L_2 edge XANES spectra of Pt and Pt-Sn alloys. A gradual increase of white line intensity as Sn content increases indicates the strong involvement of Pt 5d electron ($5d^{3/2}$) to Pt-Sn bond formation, which induces the increase of unoccupied d states, however no significant changes were observed in edge energies. The ΔXANES spectra (in inset of Figure 3 (B)) more clearly show the dependency of Pt L_2 feature on Sn addition. Since the L_3 edge transition involved Pt $5d^{5/2}$ and $5d^{3/2}$ while the Pt L_2 edge transition only involved $5d^{3/2}$, the change shown in XANES features at the Pt L_2 and Pt L_3 edge indicates clear evidence of electronic state change in Pt $d^{5/2}$ and $d^{3/2}$. Unfilled Pt $d^{5/2}$ electrons tend to be hybridized and develop various energy states with Sn addition. The Pt $d^{3/2}$ electrons, on the other hand, were directly donated to the Pt-Sn bond formation, which causes a higher degree of vacancies.

Figure 4 shows the *in situ* Pt L_3-edge XANES data of Pt-Sn/SiO_2 bimetallic catalysts in the temperature range of 25 – 600 °C at 750 psi with n-dodecane. At room temperature, the monometallic Pt catalyst shows a high degree of oxidation indicated from high binding energy shifts and the white line intensity, as shown in Figure 4(A). The white line intensity reduced significantly as the reaction temperature reached ~200 °C, indicating the increased metallic phase of Pt nanoparticles. In the case of Sn addition (< 40 wt%), the Pt_3Sn_1 catalyst shows very similar energies and white line intensities, while showing less oxidized Pt in the initial state compared to the catalyst without Sn. It is worth noting that Pt-Sn catalysts are more resistant to be oxidized as shown in the initial states (at 25 °C) of Pt_1Sn_1 and Pt_1Sn_3 catalysts. The Pt L_3 X-ray absorption is related to the chemical environment in addition to the d-

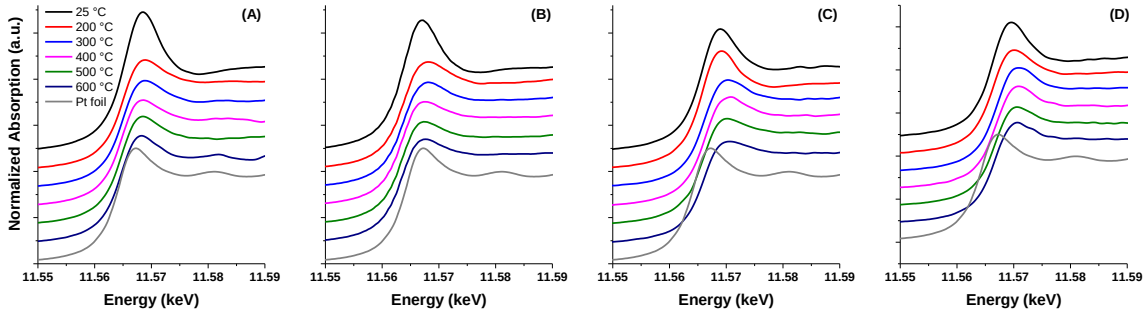

Figure 4. *In situ* Pt L_3 XANES data of Pt-Sn/SiO_2 catalysts (A) Pt (B) Pt_3Sn_1 (C) Pt_1Sn_1 (D) Pt_1Sn_3 with n-dodecane present.

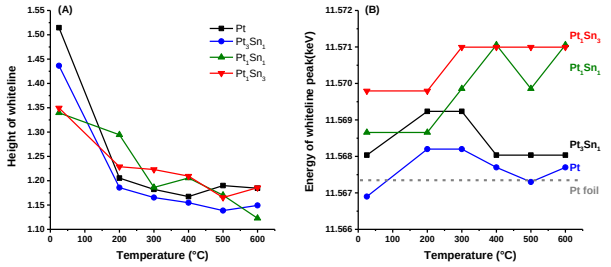

Figure 5. The heights of whiteline (A) and the peak positions of whileline (B) change over the range of temperatures.

electron valences ($5d^{3/2}$ and $5d^{5/2}$). The lower intensity of white line and higher edge energies observed for Pt_1Sn_1 and Pt_1Sn_3 catalysts, shown in Figure 4(C) and (D), suggests significant changes in their electronic properties. The intensity of white line and the peak position change under supercritical reaction environments, as clearly shown in Figure 5. The position of white line peak shifts over 4 eV for the highest amount of Sn added catalysts such as Pt_1Sn_3, compared to that of Pt foil. Kim et al. reported that the position of the white line shifts to a higher energy for Pt-Sn/C catalysts than that of Pt/C catalyst, which was attributed to partial filling of the unoccupied Pt 5d orbitals by electron donation from Sn.[35] Interestingly, the white line intensities appeared to increase as the amount of Sn increases over temperature range of 200 – 600 °C. This phenomenon is in agreement with Uemura et al.'s findings, suggesting the formation of an alloy between Pt and Sn, which has a lower electronegativity (1.9) than Pt (2.2).[36] Based on previous work on quantum chemical density functional theory (DFT) calculation and XANES analysis, the re-hybridization between the d-orbital of Pt and the valence orbitals of Sn was proposed.[37] Additional information on the effect of adsorbates on the L_3 XANES of Pt-Sn/SiO_2 catalysts, except of Pt_3Sn_1, was determined at room temperature and in the presence of air, He and toluene, shown in Figure S5. The decrease in the intensity and the shift to the higher energy of white line peaks as the amount of Sn increases indicate that the presence of adsorbates[38] is also strongly related to the degree of oxidation and final electronic state of the catalysts, which are in agreement with the XANES results in Figure 5. While the ability to control the features of the bimetallic catalysts has been exploited in extensive studies, the structural and compositional changes under endothermic reaction conditions are still a subject of debate. Zhu and coworkers have reported that the catalyst preparation method affects the distributions of Pt-Sn particle size and location, which can influence the stability and the resulting performance of the catalysts.[39] The effect of Sn loading on the dehydrogenation of alkane has revealed the increased catalyst stability and olefin selectivity due to the increased Pt metal dispersion with Sn.[20] However, to the best of our knowledge, many studies have been focused on the basic electronic or structural properties of catalysts, while none of the studies address the characteristics of Pt-Sn catalysts under supercritical reaction conditions. Therefore, from a practical point of view, our finding is the first attempt to provide the physical properties of Pt-Sn bimetallic catalysts in this demanding environment.

Table 2. Raman band position and intensity ratios for carbonaceous materials over Pt-Sn/SiO_2 catalysts

Catalyst	Sn amount (%)	G band (cm^{-1})	D_1 band (cm^{-1})	I_{D1}/I_G	I_{D3}/I_G	I_{D4}/I_G
Pt	0	1594	1338	0.64	0.19	0.29
Pt_3Sn_1	25	1595	1339	0.67	0.19	0.33
Pt_1Sn_1	50	1593	1333	0.70	0.20	0.26
Pt_1Sn_3	75	1593	1346	0.54	0.28	0.44

A major challenge of catalytic cracking is the deactivation of metal catalysts which is mainly caused by the build-up of carbonaceous deposits or coke.[40] The spent Pt-Sn bimetallic catalysts were further studied by Raman spectroscopy to analyze the coke formed during catalytic reactions.[41] Figure 6 shows the Raman spectra of coke formed over the spent catalysts (black circle). Two distinguishable Raman bands were characterized at around 1340 and 1595 cm^{-1}, identified as ring stretches of disordered (D_1 band) and ordered graphite lattice (G band), respectively.[42] The G band at 1595 cm^{-1} indicates the formation of small graphitic crystallites since the perfect graphite crystals are measured at 1575 cm^{-1}. It is well known that in Raman spectra there are 4-5 overlapping bands in carbonaceous materials. Finally, the deconvoluted Raman spectra of spent catalysts show a combination of four fitted Raman bands (Figure 6). The two additional bands, D_3 (ca. 1500 cm^{-1}) and D_4 (ca. 1200 cm^{-1}) correspond to amorphous carbon

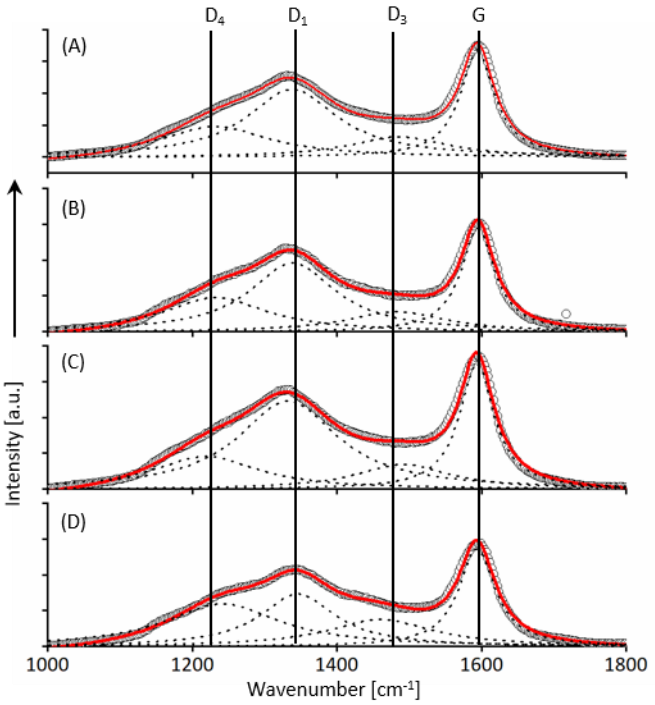

Figure 6. Deconvoluted Raman spectra of the carbon deposits formed over the spent Pt-Sn/SiO_2 catalysts, (A) Pt (B) Pt_3Sn_1 (C) Pt_1Sn_1 (D) Pt_1Sn_3, (Red line: fitted data, Black circle: Raman data)

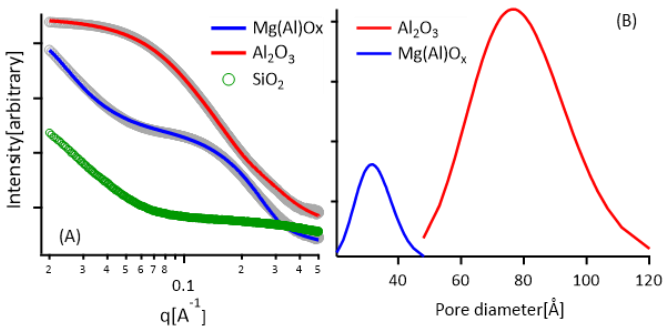

Figure 7. (A) SAXS scattering profiles of support materials, γ-Al_2O_3, $Mg(Al)O_x$ and SiO_2 in the ambient condition (gray circles: raw data, colored lines: model fitting results); (B) for the corresponding pore size distributions, note that SiO_2 is non-porous.

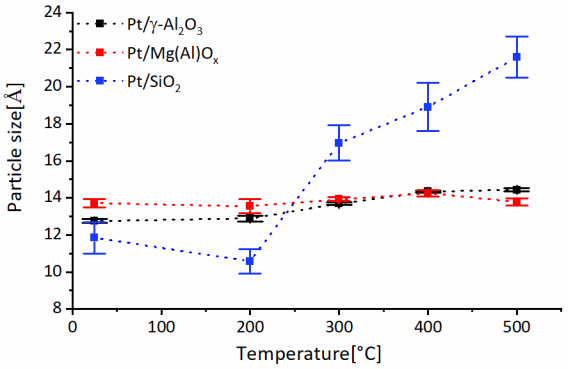

Figure 8. Variation of particle size of Pt catalyst supported on SiO_2,[9] γ-Al_2O_3 and $Mg(Al)O_x$, in the temperature range of 25 to 500 °C at 750 psi with n-dodecane

and disordered graphitic lattice (A_{1g} symmetry), respectively. There are no significant shifts observed in the position of the G band, while the D_1 bands shift with increasing amount of Sn in the catalyst. Previous work on carbon materials reveals that the shift of D_1 bands appears to result from the size variation of graphite microcrystallites.[43] The intensity ratios, D-to-G, have been used to determine the degree of graphitization of cokes[44] as listed in Table 2. The relative intensity of D_1/G was observed to decrease when the amount of Sn increases, while D_3/G and D_4/G intensity ratios showed the opposite trend. Previous studies have showed that the decreasing I_{D1}/I_G value indicates increasing degree of graphitization.[42] In our study, the increased amount of Sn may inhibit the formation of disordered graphite lattice (i.e., graphene edges), thus showing the increased graphitization of carbonaceous materials over the catalyst surface.

The results of the supercritical cracking reaction runs were analyzed in terms of reactant conversion and product selectivity. In this study, the quasi-quantitative analysis was performed due to irretrievable gas products with supercritical flow reactor. The liquid products collected at each reaction temperature were identified and analyzed by means of a GC-MSD as described elsewhere.[4] The Pt_3Sn_1 catalyst showed the highest conversion while the least among the prepared catalysts was Pt_1Sn_3 with a 35.9 % conversion as shown in Figure S6, which is in agreement with the recent findings for propane catalytic dehydrogenation.[20] The selectivity of the cracking reaction was also determined by means of the relative yields of paraffin, olefin, and aromatic compounds, in the liquid products collected at each reaction condition (Table S2 and Figure S7). The olefin compounds were dominant for the monometallic Pt catalyst while high aromatic selectivity was observed for the bimetallic catalysts. Our finding suggests that the addition of Sn may influence the cracking mechanism and the amount of Sn might be critical to prevent the formation of coke precursors. Further studies on coke formation such as total organic carbon (TOC) analysis of coke will be needed to address this issue.

3.2 Influence of support materials

SAXS measurements were performed to characterize the nanostructure of both γ-Al_2O_3 and $Mg(Al)O_x$ supports, at ambient condition. Figure 7 shows SAXS scattering profiles of two support materials and the corresponding pore size distributions. A broad scattering peak appears in the relatively high q region (q = 0.1~0.2 $Å^{-1}$) for $Mg(Al)O_x$ while observed in the q range lower than 0.1 $Å^{-1}$ for γ-Al_2O_3. Each peak was fitted to Schultz-Zimm distribution of spherical structure with aspect ratio of 0.47- 0.65. The corresponding pore diameters are 76.6 ± 1.6 for γ-Al_2O_3 and 36.7 ± 0.8 Å for and $Mg(Al)O_x$, which are well agreed to those recently reported.[29] Similar SAXS profiles with Pt supported catalysts, Pt/γ-Al_2O_3 and Pt/$Mg(Al)O_x$ were observed in the temperature range of 25 – 500 °C at 750 psi pressure with n-dodecane. No additional features were found after adding Pt, suggesting the highly dispersed Pt or the relatively small metallic contents on the supports.[45] Each SAXS intensity was fitted to clarify the changes of size and distribution of Pt catalysts during reaction as shown in Figure S8. Figure 8 represents the variation of particle size (mean diameter, Å) of Pt catalysts as the reaction temperature increases. The particle size of Pt/γ-Al_2O_3 catalyst was slightly increased from 12.8 ± 0.1 Å at 25 °C to 14.4 ± 0.1 Å at 500 °C. The particle sizes of Pt/$Mg(Al)O_x$ catalysts, however, even after the temperature reached over the supercritical condition (at 500 °C), were merely changed to 13.8 ± 0.2 Å from 13.7 ± 0.2 Å at 25 °C. There was the sudden increase on particle size of Pt/SiO_2 catalyst when the reaction condition reaches supercritical regime. As expected, both catalysts appeared relatively stable under supercritical reaction conditions compared to the changes of particle size on Pt/SiO_2 catalyst.[46] The lack of significant changes in the corresponding size distribution profiles in Figure S9 also suggests that both catalysts were stable under supercritical environment.

For the better understanding of the interplay between morphology and catalytic reaction under supercritical environment, XANES characterization has exploited to measure the electronic states above the Fermi level localized on Pt element. Figure 9 shows in situ Pt L_3-edge XANES data of Pt/γ-Al_2O_3 and Pt/$Mg(Al)O_x$ catalysts in the temperature range of 25 – 500 °C at 750 psi with n-dodecane. The white line peak is defined as the strong peak above the edge energy and it is one of an important parameter in catalytic reaction since it is mainly associated with density of vacant 5d electronic states of Pt. At room temperature, both Pt/γ-Al_2O_3 and Pt/$Mg(Al)O_x$ catalysts show high degree of oxidation indicated from high binding energy shifts and the white line intensities as shown in Figure

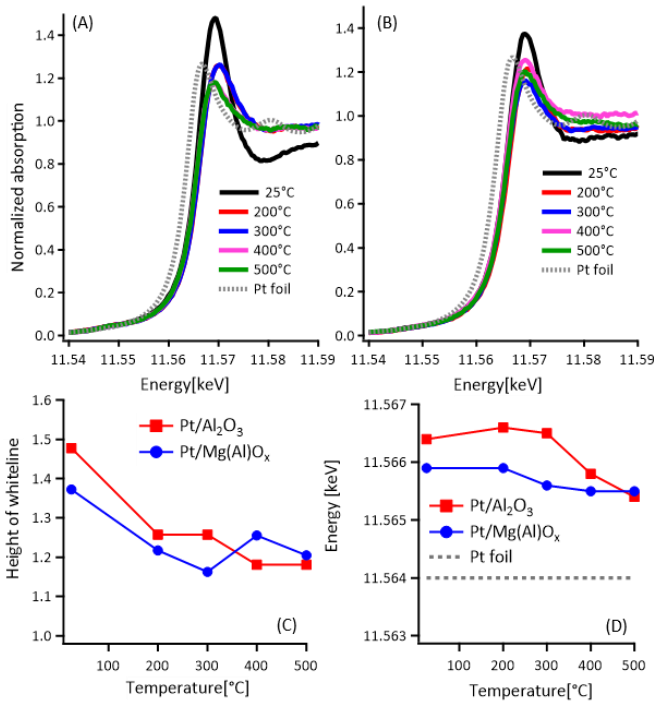

Figure 9. *in situ* Pt L_3 XANES data of Pt catalyst supported on (A) γ-Al_2O_3 and (B) $Mg(Al)O_x$ under given reaction conditions with n-dodecane (C) the height of white line and (D) the edge energy change over the range of temperatures

9(A) and (B). Larger white line intensity compared to that of $Mg(Al)O_x$ suggests a high degree of oxidation of Pt with γ-Al_2O_3 support. In Figure 9(C), the white line intensity reduced significantly as the reaction temperature reached ~200 °C, indicating the increased metallic phase of Pt nanoparticles. The variation of edge energy shows similar trend with the white line intensity in Figure 9(D). At room temperature, larger edge energy shift observed for Pt/γ-Al_2O_3 (ΔE = 2.4 eV) than that with Pt/$Mg(Al)O_x$ (ΔE = 1.9 eV) suggests significant difference of electronic properties on their metal-oxide interactions. The edge energies change over the range of temperatures under supercritical condition. Despite of no significant differences on the Pt particle size of both catalysts observed in Figure 8, the distinction of XANES results suggests the considerable influence of support material on prepared Pt catalysts by altering the electronic states. These discrepancy between Pt/γ-Al_2O_3 and Pt/$Mg(Al)O_x$ was well agreed to the catalytic performance results which obtained by quasi-quantitative analysis. A comparably high conversion was obtained at 400 °C with Pt/$Mg(Al)O_x$ catalyst (8.3 %) while 1.6 % of conversion was obtained with Pt/γ-Al_2O_3. The paraffin compounds were dominant with Pt/γ-Al_2O_3 catalyst, while the high olefin selectivity was observed with Pt/$Mg(Al)O_x$ catalyst as increased temperature at 500 °C, as shown in Figure S10. The support materials modify the mechanism of the catalytic process, influencing the properties of final products.[47] The hydrotalcite precursor derived Mg(Al)O oxides, used in this work, has shown moderate basicity and stronger Pt-support interaction than Al_2O_3.[9, 15, 48] Our findings suggest that the reactivity may be greatly influenced by the Mg/Al ratio of Pt support.

Conclusions

The present findings suggest that the physicochemical characteristics, such as particle size, morphology or electronic structure, of supported Pt catalysts are strongly affected by neighboring nanoparticles and the oxide supports under realistic reaction conditions. First, the effect of Sn loading on Pt-Sn/SiO_2 bimetallic catalysts was studied for the catalytic dehydrogenation and cracking of hydrocarbon fuels under supercritical reaction conditions. *In situ* SAXS characterization of dehydrogenation and catalytic cracking of n-dodecane over Pt and Pt-Sn catalysts has been conducted. The addition of Sn increases the stability of catalysts, with the smallest changes in metal particle size distributions observed for the Pt_1Sn_3 catalyst, which has the highest amount of Sn among the prepared catalysts. *In situ* XANES analysis shows a decrease in intensity and a shift to higher energy of the white line peaks with increasing Sn content, thereby indicating that the degree of oxidation and final electronic state of catalysts are strongly dependent on the amount of Sn in the catalysts. Two distinguishable Raman features from carbonaceous compounds were found with spent Pt-Sn catalysts, revealing the increased graphitization of carbonaceous materials over the catalyst surface as increased amount of Sn. The catalytic activity increased by adding Sn, and a high aromatic selectivity was observed with increased Sn amount, while olefin compounds were dominant with the monometallic catalyst. The results support a reaction mechanism,[42] where the formation of a disordered graphite lattice over the catalyst surface is decreased with increasing Sn content in the catalyst. Second, two supports, γ-Al_2O_3 and $Mg(Al)O_x$ have been employed to elucidate the characteristic of Pt particles on the catalytic cracking of n-dodecane at 750 psi under supercritical conditions. *In situ* SAXS characterization shows that the changes of particle size and distribution upon the temperature increases. No significant changes appeared on both the particle size and its distribution profile suggest that both catalysts were stable under supercritical environment. In situ XANES analysis reveals high degree of oxidation of Pt over γ-Al_2O_3 than $Mg(Al)O_x$ support at room temperature. Similar trends on the white line intensity and the edge energy over given conditions observed on both catalysts, however, the distinction of XANES results suggests the considerable influence of support material on prepared Pt catalysts. The catalytic performance was evaluated by quasi-quantitative GC-MSD analysis of liquid products collected each reaction conditions. The catalytic cracking with Pt/$Mg(Al)O_x$ shows high conversion at comparably low temperature under supercritical condition. The high olefin selectivity was also observed with $Mg(Al)O_x$ support at 500 °C, indicating that support may modify the mechanism of the catalytic process. The findings presented here could lead to a fundamentally new level of understanding of nanoscale materials by monitoring the catalysts under realistic reaction conditions.

Conflicts of interest

There are no conflicts to declare.

Acknowledgements

This work was supported by Air Force Office of Scientific Research through Basic Research Initiative grant AFOSR FA9550-12-1-0400 and AFOSR FA9550-16-1-0141. The use of 12-BM beamline of the Advanced Photon Source is supported by the U.S. Department of Energy (DOE) Office of Science User Facility operated for the DOE Office of Science by Argonne National Laboratory under Contract No. DE-AC02-06CH11357.

References

1. T. Edwards, *Combust Sci. Technol.*, 2006, **178**, 307-334.
2. N. Gascoin, P. Gillard, E. Dufour and Y. Touré, *J. Thermophys. Heat Tr.*, 2007, **21**, 86-94.
3. Y. Jiao, J. Wang, Q. Zhu, X. Li and Y. Chen, *Energy Fuels*, 2014, **28**, 5382-5388.
4. G. Liu, Y. Han, L. Wang, X. Zhang and Z. Mi, *Energy Fuels*, 2009, **23**, 356-365.
5. B. D. Beaver, C. B. Clifford, M. G. Fedak, L. Gao, P. S. Iyer and M. Sobkowiak, *Energy Fuels*, 2006, **20**, 1639-1646.
6. G. Liu, Y. Han, L. Wang, X. Zhang and Z. Mi, *Energy Fuels*, 2008, **22**, 3960-3969.
7. S. Tang, S. Gao, S. Hu, J. Wang, Q. Zhu, Y. Chen and X. Li, *Ind. Eng. Chem. Res.*, 2014, **53**, 5432-5442.
8. M. M. Bhasin, J. H. McCain, B. V. Vora, T. Imai and P. R. Pujadó, *Appl. Catal. A-Gen.*, 2001, **221**, 397-419.
9. S. Lee, S. Lee, M. D. Kumbhalkar, K. M. Wiaderek, J. Dumesic and R. E. Winans, *ChemCatChem*, 2017, **9**, 99-102.
10. H.-C. Wu, T.-C. Chen, Y.-C. Chen, J.-F. Lee and C.-S. Chen, *J. Catal.*, 2017, **355**, 87-100y.
11. O. A. Bariås, A. Holmen and E. A. Blekkan, *J. Catal.*, 1996, **158**, 1-12.
12. L.-L. Shen, K. Xia, W.-Z. Lang, L.-F. Chu, X. Yan and Y.-J. Guo, *Chem. Eng. J.*, 2017, **324**, 336-346.
13. C. Sun, J. Luo, M. Cao, P. Zheng, G. Li, J. Bu, Z. Cao, S. Chen and X. Xie, *J. Energy Chem.*, 2018, **27**, 311-318.
14. F. Meemken, N. Maeda, K. Hungerbühler and A. Baiker, *Angew. Chem. Int. Edit.*, 2012, **51**, 8212-8216.
15. S. Rauch, H. F. Hemond, C. Barbante, M. Owari, G. M. Morrison, B. Peucker-Ehrenbrink and U. Wass, *Environ. Sci. Technol.*, 2005, **39**, 8156-8162.
16. A. Iglesias-Juez, A. M. Beale, K. Maaijen, T. C. Weng, P. Glatzel and B. M. Weckhuysen, *J. Catal.*, 2010, **276**, 268-279.
17. A. W. Hauser, J. Gomes, M. Bajdich, M. Head-Gordon and A. T. Bell, *Phys. Chem. Chem. Phys.*, 2013, **15**, 20727-20734.
18. J. Wu, Z. Peng and A. T. Bell, *J. Catal.*, 2014, **311**, 161-168.
19. E. Merlen, P. Beccat, J. C. Bertolini, P. Delichère, N. Zanier and B. Didillon, *J. Catal.*, 1996, **159**, 178-188.
20. M.-H. Lee, B. M. Nagaraja, K. Y. Lee and K.-D. Jung, *Catal. Today*, 2014, **232**, 53-62.
21. Y. Lai, S. He, X. Li, C. Sun and K. Seshan, *Appl. Catal. A-Gen.*, 2014, **469**, 74-80.
22. A. B. Merlo, B. F. Machado, V. Vetere, J. L. Faria and M. L. Casella, *Appl. Catal. A-Gen.*, 2010, **383**, 43-49.
23. W. D. Michalak, J. M. Krier, S. Alayoglu, J.-Y. Shin, K. An, K. Komvopoulos, Z. Liu and G. A. Somorjai, *J. Catal.*, 2014, **312**, 17-25.
24. R. M. Watwe, R. D. Cortright, M. Mavrikakis, J. K. Nørskov and J. A. Dumesic, *J. Chem. Phys.*, 2001, **114**, 4663-4668.
25. D. Gerceker, A. H. Motagamwala, K. R. Rivera-Dones, J. B. Miller, G. W. Huber, M. Mavrikakis and J. A. Dumesic, *ACS Catal.*, 2017, **7**, 2088-2100.
26. H. Armendáriz, A. Guzmán, J. A. Toledo, M. E. Llanos, A. Vázquez and G. Aguilar-Ríos, *Appl. Catal. A*, 2001, **211**, 69-80.
27. S. He, C. Sun, Z. Bai, X. Dai and B. Wang, *Appl. Catal. A-Gen.*, 2009, **356**, 88-98.
28. S. Fang, K. Bi, Q. Zhang, L. Chen, Y. Sun, H. Huang, L. Ma and C. Wang, *Catalysts*, 2018, **8**, 296.
29. O. B. Belskaya, L. N. Stepanova, T. I. Gulyaeva, D. V. Golinskii, A. S. Belyi and V. A. Likholobov, *Kinet. Catal.*, 2015, **56**, 655-662.
30. J. G. Moya-Cancino, A.-P. Honkanen, A. M. J. van der Eerden, H. Schaink, L. Folkertsma, M. Ghiasi, A. Longo, F. M. F. de Groot, F. Meirer, S. Huotari and B. M. Weckhuysen, *ChemCatChem*, **11**, 1-7.
31. D. Sun, C. Li, Y. Du, L. Kou, J. Zhang, Y. Li, Z. Wang, J. Li, H. Feng and J. Lu, *Fuel*, 2019, **239**, 659-666.
32. H. A. Benesi, R. M. Curtis and H. P. Studer, *J. Catal.*, 1968, **10**, 328-335.
33. J. Ilavsky and P. R. Jemian, *J. Appl. Crystallogr.*, 2009, **42**, 347-353.
34. B. Ravel and M. Newville, *J. Synchrotron Radiat.*, 2005, **12**, 537-541.
35. J. H. Kim, S. M. Choi, S. H. Nam, M. H. Seo, S. H. Choi and W. B. Kim, *Appl. Catal. B-Environ.*, 2008, **82**, 89-102.
36. Y. Uemura, Y. Inada, K. K. Bando, T. Sasaki, N. Kamiuchi, K. Eguchi, A. Yagishita, M. Nomura, M. Tada and Y. Iwasawa, *Phys. Chem. Chem. Phys.*, 2011, **13**, 15833-15844.
37. H. Xin, A. Holewinski, N. Schweitzer, E. Nikolla and S. Linic, *Top. Catal.*, 2012, **55**, 376-390.
38. Y. Lei, J. Jelic, L. C. Nitsche, R. Meyer and J. Miller, *Top. Catal.*, 2011, **54**, 334-348.
39. H. Zhu, D. H. Anjum, Q. Wang, E. Abou-Hamad, L. Emsley, H. Dong, P. Laveille, L. Li, A. K. Samal and J.-M. Basset, *J. Catal.*, 2014, **320**, 52-62.
40. J. McGregor, Z. Huang, E. P. J. Parrott, J. A. Zeitler, K. L. Nguyen, J. M. Rawson, A. Carley, T. W. Hansen, J.-P. Tessonnier, D. S. Su, D. Teschner, E. M. Vass, A. Knop-Gericke, R. Schlögl and L. F. Gladden, *J. Catal.*, 2010, **269**, 329-339.
41. Z. Han, S. Li, F. Jiang, T. Wang, X. Ma and J. Gong, *Nanoscale*, 2014, **6**, 10000-10008.
42. J. J. H. B. Sattler, A. M. Beale and B. M. Weckhuysen, *Phys. Chem. Chem. Phys.*, 2013, **15**, 12095-12103.
43. Y. Wang, D. C. Alsmeyer and R. L. McCreery, *Chem. Mater.*, 1990, **2**, 557-563.
44. J. Yu, L. Sun, J. Xiang, S. Hu, S. Su and Y. Wang, *Energy Fuels*, 2014, **28**, 7235-7242.
45. F. Chen, G. Wang, W. Li and F. Yang, *Ind. Eng. Chem. Res.*, 2013, **52**, 565-571.
46. S. Nishimura, A. Takagaki and K. Ebitani, *Green Chem.*, 2013, **15**, 2026-2042.
47. Y. Zhang, Y. Zhou, K. Yang, Y. Li, Y. Wang, Y. Xu and P. Wu, *Micropor. Mesopor. Mat.*, 2006, **96**, 245-254.

48. J. Luo, F. Gao, A. M. Karim, P. Xu, N. D. Browning and C. H. F. Peden, *ACS Catal.*, 2015, **5**, 4680-4689.

Table of Contents

Investigation of the size and structure of supported Pt catalysts under supercritical conditions leads to fundamentally new level of understanding of nanoscale materials under extreme conditions.